3D PRINTING

A silicone-based support material eliminates interfacial instabilities in 3D silicone printing

Senthilkumar Duraivel[1], Dimitri Laurent[2], Didier A. Rajon[2], Georg M. Scheutz[3], Abhishek M. Shetty[4], Brent S. Sumerlin[3], Scott A. Banks[5], Frank J. Bova[2], Thomas E. Angelini[1,5,6]*

Among the diverse areas of 3D printing, high-quality silicone printing is one of the least available and most restrictive. However, silicone-based components are integral to numerous advanced technologies and everyday consumer products. We developed a silicone 3D printing technique that produces precise, accurate, strong, and functional structures made from several commercially available silicone formulations. To achieve this level of performance, we developed a support material made from a silicone oil emulsion. This material exhibits negligible interfacial tension against silicone-based inks, eliminating the disruptive forces that often drive printed silicone features to deform and break apart. The versatility of this approach enables the use of established silicone formulations in fabricating complex structures and features as small as 8 micrometers in diameter.

Silicone elastomer's resistance to heat, chemical agents, weathering, ozone, moisture, and ultraviolet (UV) irradiation makes it critical for manufacturing countless products, including electronic devices, automobiles, aircraft, and medical devices (*1*). Silicone elastomers have been used in medical devices for many years (*2*), and their applications include embedded sensors (*3*), flexible electronics (*4*), soft robotics (*5*), and additive manufacturing (*6*). Silicone structures can be fabricated by using conventional techniques such as molding, or advanced techniques such as soft lithography and 3D printing (*7*–*9*). However, 3D printing with silicone generally results in low-quality products because of challenges created by the interfacial behaviors of silicone pre-elastomer in its liquid state. These challenges can be partially addressed by using an embedding support material that flows around the translating printing nozzles while trapping deposited inks in space, providing stability to printed structures (*10*–*14*). However, even under such stabilizing conditions, the interfacial tension between printed inks and their support media drives the deformation and breakup of printed structures before they solidify (Fig. 1, A and B) (*9*, *15*). Modifying silicone inks with additives can stabilize 3D printed structures (*16*, *17*), yet a versatile approach to additive manufacturing with unmodified silicone inks remains elusive. One route to achieving high-quality 3D silicone printing without ink modification is to eliminate the disruptive role of interfacial tension by using support materials that are chemically similar to the printed inks they stabilize (Fig. 1C). Thus, there is a critical need to develop support materials that are chemically similar to poly(dimethylsiloxane) (PDMS) inks.

We describe a method for 3D printing precise, intricately detailed structures made from PDMS that makes use of a support material exhibiting negligible interfacial tension when in contact with silicone inks. We call this method additive manufacturing at ultralow interfacial tension (AMULIT). The AMULIT support material is a packed inverse emulsion composed of aqueous droplets in a continuum of silicone oil. The ultralow interfacial tension between the AMULIT support material and PDMS inks enabled us to print features with diameters as small as 8 μm. We achieved high-performance printing by tuning the elasticity and flow properties of this support material, which allowed us to fabricate complicated shapes such as brain aneurysm models and functional trileaflet heart valves. We demonstrated that the AMULIT technique does not require specialized inks by using several different commercially available PDMS formulations to print various structures. With mechanical testing, we found that 3D printed structures produced by using AMULIT were more extensible than their molded counterparts and equally robust. We also found that these structures have a smooth surface finish at the macroscale and microscale roughness, which is facilitated by the low interfacial tension between PDMS inks and the AMULIT support medium. Our results show that the AMULIT 3D printing technique could be used to fabricate intricate silicone structures for biomaterial design and surgical simulators, and they introduce the possibility of expanding the method for printing with other materials.

[1]Department of Materials Science and Engineering, University of Florida, Gainesville, FL 32603, USA. [2]Department of Neurosurgery, University of Florida College of Medicine, Gainesville, FL 32608, USA. [3]George and Josephine Butler Polymer Research Laboratory, Center for Macromolecular Science and Engineering, Department of Chemistry, University of Florida, Gainesville, FL 32611, USA. [4]Advanced Technical Center, Anton Paar USA, Ashland, VA 23005, USA. [5]Department of Mechanical and Aerospace Engineering, University of Florida, Gainesville, FL 32611, USA. [6]J. Crayton Pruitt Family Department of Biomedical Engineering, University of Florida, Gainesville, FL 32611, USA.
*Corresponding author. Email: t.e.angelini@ufl.edu

Results

Formulation and testing of AMULIT support material

To formulate an AMULIT support medium for 3D printing with PDMS inks, we prepared inverse emulsions in which silicone oil was the continuous phase and varied the aqueous droplet packing fraction, ϕ, and the average droplet radius, a, between samples; ϕ and a can be tuned independently to determine an emulsion's rheological properties and its corresponding performance as a printing support medium (*18*). We expected a to strongly influence the printed feature roughness because the material interfaces will not spontaneously flatten under conditions of ultralow interfacial tension. Thus, we formulated small emulsion droplets and chose ϕ on the basis of the emulsions' rheological properties (fig. S1). The elastic shear modulus, G', and yield stress, σ_y, of each formulation, were measured with rheological tests (materials and methods and fig. S2). For AMULIT printing, we chose an emulsion having σ_y = 9 Pa and G' = 320 Pa; the emulsion with these properties is weak enough to flow around a translating printing needle yet strong enough to support complex 3D printed structures (*9*, *10*). For this formulation, we estimated the Reynolds number near the translating nozzle during a typical print to be 10^{-6} to 10^{-2}, which indicates that irregular flow patterns should be suppressed (supplementary text). For all formulations, we found that emulsions made from pure water droplets in silicone oil were extremely cloudy and inhibited visualizing the printing process. To make optically clear emulsions, we matched the refractive indices of the two phases by adding glycerol to the droplets, which allowed the 3D printing process to be imaged at the macroscale with photography and at the microscale with confocal fluorescence microscopy (CFM) (Fig. 1, D to G, and fig S3).

To test the role of interfacial tension in embedded 3D printing, we compared the performance of the AMULIT support medium with an all-aqueous support medium made from packed hydrogel microparticles swollen in water. In both cases, we 3D printed features made from a fluorescent PDMS liquid and imaged the ink-support interfaces using CFM (materials and methods). We formulated the packed microgels to have σ_y = 10 Pa and G' = 550 Pa, values comparable to those of the AMULIT material. Examining the 3D fluorescence images, we found that printed silicone features broke up and formed spherical droplets within the aqueous support. When a liquid ink is printed into a packed granular support medium, the smallest stable feature has a diameter given by $d_{min} \approx 2\gamma/\sigma_y$, where γ is the interfacial tension between the ink and the support medium (*15*). For the aqueous medium, γ = 25 mN/m, so d_{min} was ≈5 mm,

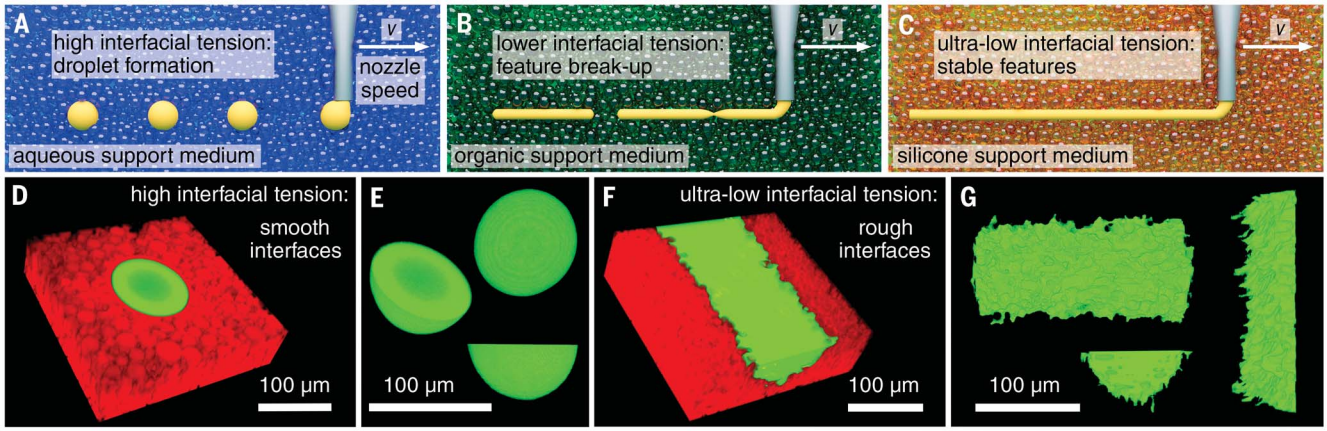

Fig. 1. Interfacial tension drives feature breakup in embedded 3D printing. (**A**) High interfacial tension between aqueous support materials and silicone inks destabilizes 3D printed features, driving them to break into spherical droplets. (**B**) Intermediate interfacial tension between organic support materials and silicone inks provides some stability but limits minimum stable feature size. (**C**) Ultralow interfacial tension between silicone oil–based support materials and silicone inks eliminates interfacial instabilities, removing the limits on minimum stable feature size. (**D**) CFM image showing silicone-based inks (green) that break into droplets when printed into support materials made from aqueous microgels (red). (**E**) A droplet digitally isolated from the support and examined from different angles. The droplet appears nearly spherical and exhibits a smooth surface. (**F**) By contrast, the silicone-based ink (green) remains continuous and retains its shape indefinitely after printing into a silicone-based support material (red). (**G**) When viewed from different angles, the printed features exhibit roughness with a characteristic length scale of the microparticles composing the support material, facilitated by ultralow interfacial tension.

50 times the 100-μm diameter of the printed feature (Fig. 1, D and E). Thus, the breakup of the feature into droplets was expected. By contrast, the 100-μm diameter silicone feature printed into the AMULIT support material remained intact, indicating that $\gamma < 0.5$ mN/m. To better estimate γ between a PDMS ink and the AMULIT support medium, we performed a series of test prints in which d_{min} was measured for multiple values of σ_y, finding that $\gamma \approx 0.08$ mN/m (fig. S4). We also observed that the characteristic roughness length scale at the feature surface was about one order of magnitude smaller than the feature diameter, from which we would estimate $\gamma \approx 0.05$ mN/m. These results indicate that the AMULIT approach can potentially achieve features 300 to 500 times smaller than those achievable when printing PDMS into an aqueous support medium having the same material properties.

Complex device fabrication using the AMULIT technique

The improvement in complexity, quality, and functionality of PDMS vessel models traced in the published literature parallels a decrease in interfacial tension of silicone inks against their embedding materials. For example, hydrocarbon support materials (*9*) improved on aqueous support materials (*19*). As a first test of the AMULIT method's capabilities, we printed a model brain aneurysm; models with accurate vasculature are needed for improved patient simulators to train neurosurgeons in cerebrovascular procedures. Current simulated tissues provide unrealistic tactile feedback, lack small-diameter intracranial angioarchitecture, and often exclude the aortic arch and extracranial vascular anatomy that determine which catheters and instruments are used in each procedure (*20*, *21*).

To create a model, we collected a 3D angiogram of a patient's brain aneurysm using x-ray computed tomography (XRCT). The 3D scan was segmented and processed to create a series of 3D printing trajectories (Fig. 2A and materials and methods). We used Gelest ExSil 100 silicone pre-elastomer, which can be formulated to have material properties that mimic a wide range of tissues. A snapshot from a video of the printing process demonstrates how the translating needle flows easily through the jammed emulsion, which traps the deposited silicone in place (Fig. 2B and movie S1). The printed structure was cured at 60°C for 24 hours and then imaged with XRCT (Fig. 2C). Horizontal and vertical slices through the 3D scan revealed that the highly branched, complex printed network of vessels is hollow, with an average wall thickness of ≈400 μm (Fig. 2D and movie S2). The CT scan of the printed structure was used to create a 3D model for quantitative comparison with the original angiogram. The registration between the patient-derived model and the printed model is excellent; 68% of the printed-surface locations lie within 500 μm of their programmed locations, and 95% lie within 1 mm (Fig. 2, E and F).

Our ability to accurately model brain vasculature raises the question of whether such fine structures can be manufactured to be both highly compliant and physically robust. The artificial aortic heart valve belongs to a class of devices with such requirements. Native aortic heart valves are subject to dynamic mechanical loads during the cardiac cycle (*22*). Prosthetic replacement is widely used to treat aortic valve failure, yet the predominantly used mechanical valves and allogeneic- or xenogeneic-tissue valve replacements often result in mechanical failure, hemolysis, blood coagulation, or structural degradation due to calcification. A potential alternative is an artificial silicone valve prosthesis; silicone is established in vascular applications because of its hemocompatibility and durability (*22*–*27*). The AMULIT 3D printing method can be used to replicate the intricate semilunar shape of the thin aortic leaflets in manufactured silicone valves. We designed a model heart valve based on physiologically representative dimensions of the different valve components (Fig. 2, G and H, and fig. S5) (*28*). We used a UV-curable silicone formulation, Silopren UV Electro-225-1 (Momentive), as the ink and printed it into the AMULIT material (Fig. 2I). To create highly flexible leaflets, we printed the structure by translating the needle tip at a speed of 2 mm/s and depositing material at a rate of 125 μL/hour, producing features ≈150 μm in diameter. Correspondingly, we chose a layer spacing of 100 μm for good layer adhesion. The printed model was then UV cured, removed from the AMULIT material, washed with detergent, and rinsed in deionized water (materials and methods). The cured part had a final wall thickness of ≈250 μm. Despite having very thin, flexible walls, the model valves were physically robust enough to connect to pipe

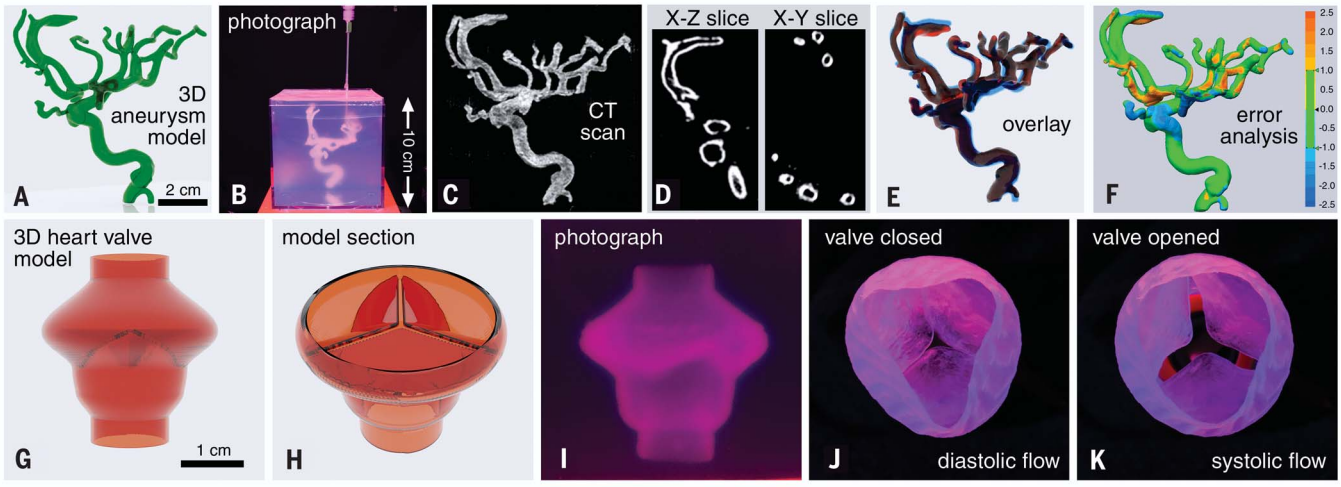

Fig. 2. AMULIT printing of brain aneurysm and aortic heart valve models. (**A**) Brain aneurysm models for surgical simulations comprise complex, interconnected, hollow tubes with intricate details. (**B**) Photograph of the aneurysm model being printed into the AMULIT material. (**C**) CT imaging of the 3D printed model within the printing container shows the complexity of the printed aneurysm. (**D**) Slices through the CT scan show that the printed structure exhibits the hollow channels of the patients' neurovasculature. (**E** and **F**) The printed structure overlays well with the patient's neurovasculature, and quantitative error analysis demonstrates agreement between the two (±1 mm error range corresponds to 95% of all points). (**G** and **H**) A model tricuspid aortic heart valve designed by using the geometric measurements of the native heart valve. (**I**) A silicone heart valve model printed in a single seamless trajectory with a wall thickness of 250 μm within the AMULIT support medium and cured under a UV lamp. (**J** and **K**) Once cured and washed, the valve model is robust enough to be coupled with a water supply, simulating transvalvular flow of the cardiac cycle. The thin leaflets of the valve are observed to open and close during the systolic and diastolic flow of the simulation.

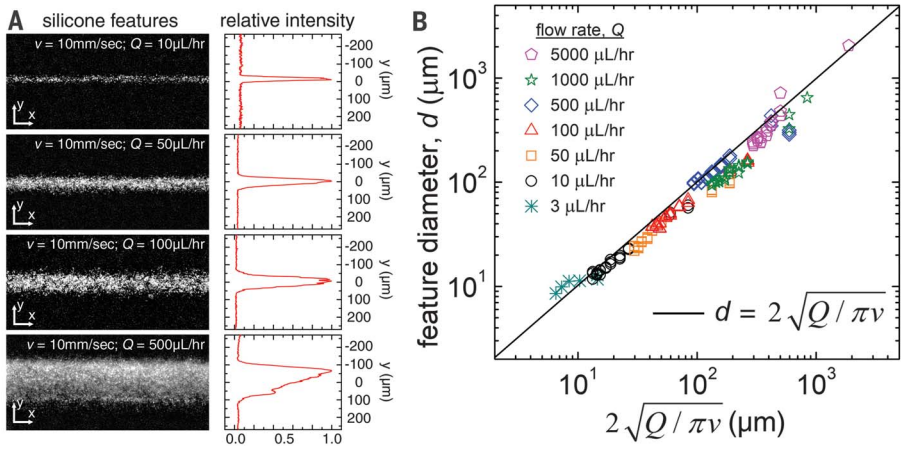

Fig. 3. Control of AMULIT printed feature size. (**A**) (Left) Intensity-inverted images. These images are averaged along the *x* axis, yielding an intensity profile across each feature. (Right) A Gaussian function is fit to the intensity profile to determine the diameter of the printed line. We measured printed feature diameter with brightfield microscopy, varying the translation speed, v, of the printing nozzle and the ink deposition rate, *Q*. (**B**) Feature diameter of the printed silicone is controllable and can be predicted from a fluid continuity equation with no fitting parameters.

fittings and simulate transvalvular blood flow through cyclic pumping of water (movie S3). During the negative flow of the pulse representing the diastolic cycle, the valves remained closed with very little deflection on the thin leaflets (Fig. 2J), and during the positive pulse corresponding to the systolic cycle, the leaflets deflected, opening the valve and letting the water flow (Fig. 2K).

AMULIT performance: Feature size and print quality

The wall thicknesses of the brain vasculature and heart valve models were set by using a combination of feature diameter and layer spacing. The feature diameter, *d*, for different prints, can be chosen by selecting a combination of nozzle translation speed, v, and material deposition rate, *Q*. To systematically explore how well *d* can be predicted with the AMULIT technique, we printed a series of linear features using the Smooth-On Mold Max 10 PDMS formulation at different combinations of v and *Q* and then measured *d* (Fig. 3A and materials and methods).We predicted the relationship between *d*, *Q*, and v, given by $\pi\,(d/2)^2 = Q/v$, according to basic fluid continuity. Performing many experiments at different combinations of *Q* and v, we found that this prediction matched the measured feature diameter very well with no adjustable parameters (Fig. 3B). These printed features were stable over time; the change in measured feature size over the course of 120 min postprinting was found to be negligible (fig. S6). We were able to fabricate stable silicone features as small as 8 μm in diameter using the AMULIT printing technique; the smallest stable feature diameter we have seen previously demonstrated with unmodified silicone was 40 μm, although smaller unstable features were also reported (*9*). A feature diameter of 10 μm was previously achieved by modifying silicone ink with emulsion droplets (*16*, *29*). To print these very fine features, we formulated an AMULIT support material with an increased yield stress using droplets 1 μm in diameter (fig. S1); the high-magnification images in Fig. 1F indicate that larger droplets would impose interfacial roughness comparable to these small feature diameters.

We have shown that highly controlled 3D printing with PDMS is possible with the AMULIT

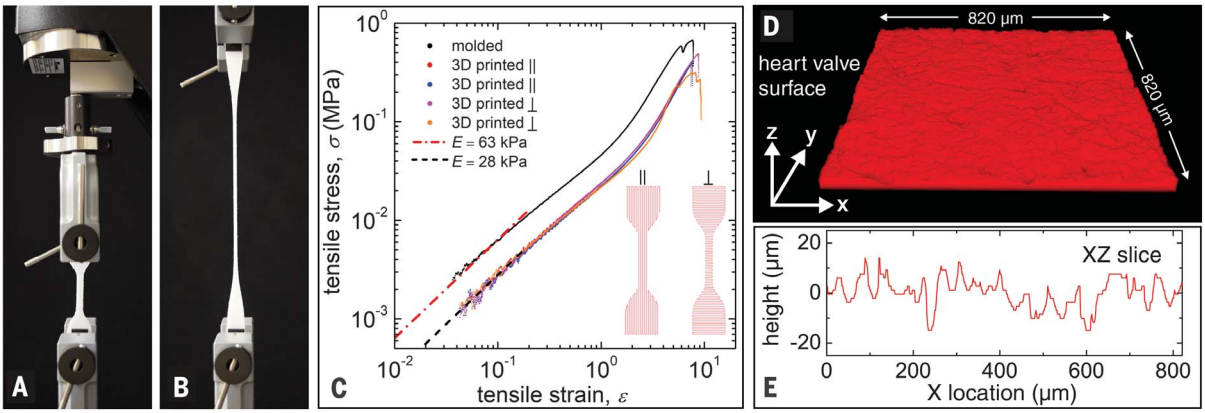

Fig. 4. Material and surface properties of the AMULIT printed silicone structures. (**A** and **B**) Silicone tensile specimens are subject to unidirectional tensile stress and are stretched to failure. (**C**) Tensile stress-strain curves of the specimens printed with their features oriented parallel and perpendicular to the tensile force show linear stress-strain relationships at low strains and exhibit an elastic modulus of 28 kPa. (**D** and **E**) Surface profiles of the printed silicone heart valves exhibit microroughness with an RMS value of 5.5 μm, likely determined by the emulsion droplet radius and the ultralow interfacial tension with the AMULIT support material.

technique, and the functionality of the heart valve model suggests that such structures may be sufficiently compliant and durable for use in applications. To test the mechanical performance of printed silicone structures, we fabricated tensile specimens using PlatSil-71 RTV (room-temperature vulcanizing) (Polytek) silicone formulation following ASTM standard D412 Type C specifications. To test the role of layer-to-layer adhesion in the mechanical integrity of the samples, we printed them with their extruded features oriented in both the longitudinal and lateral directions with respect to the long axis of the specimen geometry. The printed structures were cured at 60°C for 4 hours and then tested by using an Instron 5943 at a loading rate of 500 mm/min (Fig. 4, A and B). The tensile stress-strain data showed that both the lateral and longitudinal print specimens differed negligibly from one another and had the same elastic modulus of 28 kPa (Fig. 4C). All printed specimens exhibited linear stress-strain relationships at low strain levels and repeatable stress-strain curves at higher strains, failing at strains greater than 1000%. Comparing these results with the performance of molded specimens, we found that all the stress-strain curves had the same shape but that printed structures failed at higher strains than molded structures, whereas molded structures exhibited elastic moduli approximately twice those of printed structures. This softening effect could arise from systematic heterogeneities in the printed structures inherent to the 3D printing process. Additionally, we conducted fatigue tests, imposing 10^5 cycles of ±10% strain, alternately stretching and buckling the samples. Subsequent tensile tests showed that the printed structures exhibited less fatigue than did their molded counterparts; the elastic modulus dropped by 18% for the cast samples and 14% for the printed structures (fig. S7).

As a final assessment of the quality of structures fabricated with the AMULIT printing technique, we investigated the surface finish of fabricated parts. The ultralow interfacial tension between the silicone and the AMULIT support material was expected to produce microrough surfaces on the printed shapes. Using CFM, we imaged a segment of the heart valve model immersed in a rhodamine solution, visualizing and quantifying the surface roughness in 3D. We found the root mean square (RMS) roughness to be 6.54 ± 0.95 μm (mean and standard error, respectively) which is comparable to the average diameter of emulsion droplets used in these tests, ≈4 μm. Thus, we expect a smaller roughness with smaller emulsion droplets such as those used to print very fine features (Fig. 3B). This value is also comparable to the roughness of PDMS structures printed into support materials that exhibit a high interfacial tension against silicone inks (*9*), so it may be limited by other factors. In either case, our results demonstrate that eliminating disruptive interfacial driving forces with the AMULIT technique enables precise silicone printing without reducing surface quality or mechanical performance of fabricated structures. The added role of emulsion droplet size in surface roughness may enable a printed structure's optical properties to be tuned while independently controlling its mechanical performance through ink composition or feature diameter.

Conclusions

The AMULIT 3D printing method eliminates the disruptive effects of interfacial tension between printed inks and their support materials. Our results show that AMULIT printing can be used to make precise, smooth, strong, and functional devices from commercially available PDMS formulations. The versatility of the AMULIT technique eliminates the need to formulate specialized PDMS inks for 3D applications and broadens the toolbox for researchers and industrial manufacturers seeking to 3D print PDMS-based devices, while improving on previous silicone printing methods. The AMULIT strategy hinges on formulating support materials that are chemically similar to the inks they support—in this case, PDMS inks printed into a continuum of PDMS oil—although the same principle could be used with aqueous polymers. Despite the chemical similarity between the ink and the support medium, we never observed intermixing between the two materials that interfered with printing quality. The very low Reynolds number exhibited during embedded 3D printing with materials such as those we used should facilitate the formation of ink–support interfaces (*30*), potentially stabilized by an effective interfacial tension (*31*) or a form of liquid–liquid phase separation (*32*), likely influenced by the jammed emulsion phase. Additionally, weak attractive interactions between the emulsion droplets may help to retain them on their side of the interfaces (*33*–*35*). In the near term, we envision the AMULIT method to be useful in 3D printing for a wide range of applications beyond silicone-based devices, given the diversity and availability of polymer systems and the simplicity of formulating AMULIT support materials.

REFERENCES AND NOTES

1. H. H. Moretto, M. Schulze, G. Wagner, in *Ullmann's Encyclopedia of Industrial Chemistry* (Wiley VCH, 2011), pp. 23–26.
2. A. Rahimi, A. Mashak, *Plast. Rubber Compos.* **42**, 223–230 (2013).
3. X. Ruan *et al.*, *Adv. Mater. Technol.* **5**, 2000171 (2020).

4. A. Nathan *et al*., *Proc. IEEE* **100**, 1486–1517 (2012).
5. O. D. Yirmibeşoğlu *et al*., in *2018 IEEE International Conference on Soft Robotics* (*RoboSoft*), Livorno, Italy, 24 to 28 April 2018 (IEEE, 2018), pp. 295–302.
6. F. Liravi, E. Toyserkani, *Addit. Manuf.* **24**, 232–242 (2018).
7. V. Ozbolat *et al*., *ACS Biomater. Sci. Eng.* **4**, 682–693 (2018).
8. T. Femmer, A. J. Kuehne, M. Wessling, *Lab Chip* **14**, 2610–2613 (2014).
9. C. S. O'Bryan *et al*., *Sci. Adv.* **3**, e1602800 (2017).
10. T. Bhattacharjee *et al*., *Sci. Adv.* **1**, e1500655 (2015).
11. T. Bhattacharjee *et al*., *Soft Matter* **14**, 1559–1570 (2018).
12. G. Ovarlez, Q. Barral, P. Coussot, *Nat. Mater.* **9**, 115–119 (2010).
13. L. Mohan, C. Pellet, M. Cloitre, R. Bonnecaze, *J. Rheol.* (*N.Y.N.Y.*) **57**, 1023–1046 (2013).
14. J. R. Seth, L. Mohan, C. Locatelli-Champagne, M. Cloitre, R. T. Bonnecaze, *Nat. Mater.* **10**, 838–843 (2011).
15. C. S. O'Bryan, A. Brady-Miné, C. J. Tessmann, A. M. Spotz, T. E. Angelini, *Soft Matter* **17**, 3886–3894 (2021).
16. B. M. Rauzan, A. Z. Nelson, S. E. Lehman, R. H. Ewoldt, R. G. Nuzzo, *Adv. Funct. Mater.* **28**, 1707032 (2018).
17. C. Perrinet, E. J. Courtial, A. Colly, C. Marquette, R. Fulchiron, *Adv. Mater. Technol.* **5**, 1901080 (2020).
18. T. G. Mason, J. Bibette, D. A. Weitz, *Phys. Rev. Lett.* **75**, 2051–2054 (1995).
19. T. J. Hinton, A. Hudson, K. Pusch, A. Lee, A. W. Feinberg, *ACS Biomater. Sci. Eng.* **2**, 1781–1786 (2016).
20. M. Waqas *et al*., *Neurosurgery* **87**, E445–E453 (2020).
21. T. Scullen, J. D. Nerva, P. S. Amenta, A. S. Dumont, *Neurosurgery* **87**, E454–E455 (2020).
22. F. B. Coulter *et al*., *Matter* **1**, 266–279 (2019).
23. M. A. Punchard *et al*., *Ann. Biomed. Eng.* **37**, 1322–1330 (2009).
24. R. N. Ghriallais, L. McNamara, M. Bruzzi, *J. R. Soc. Interface* **10**, 20120965 (2013).
25. L. Rouleau, J. Rossi, R. L. Leask, *J. Biomech. Eng.* **132**, 071015 (2010).
26. J. Martorell *et al*., *Cardiovasc. Res.* **103**, 37–46 (2014).
27. M. Balcells *et al*., *Circulation* **121**, 2192–2199 (2010).
28. W. Sun, C. Martin, T. Pham, *Annu. Rev. Biomed. Eng.* **16**, 53–76 (2014).
29. Z.-T. Xie, D.-H. Kang, M. Matsusaki, *Soft Matter* **17**, 8769–8785 (2021).
30. K. J. LeBlanc *et al*., *ACS Biomater. Sci. Eng.* **2**, 1796–1799 (2016).
31. D. Truzzolillo, L. Cipelletti, *Soft Matter* **13**, 13–21 (2016).
32. S. Duraivel *et al*., *Biophys. Rev.* **3**, 031307 (2022).
33. V. V. Erramreddy, S. Ghosh, *Langmuir* **30**, 11062–11074 (2014).
34. A. Z. Nelson, R. H. Ewoldt, *Soft Matter* **13**, 7578–7594 (2017).
35. A. Z. Nelson *et al*., *Curr. Opin. Solid State Mater. Sci.* **23**, 100758 (2019).
36. S. Duraivel, T. E. Angelini, Heart Valve Maker, v2.0, Zenodo (2023); https://doi.org/10.5281/zenodo.7643835.

ACKNOWLEDGMENTS

The authors thank Anton Paar for use of their MCR 702 rheometer through the Anton Paar VIP research program. **Funding:** No funding was received. **Author contributions:** Conceptualization: S.D. and T.E.A. Methodology: S.D., D.L., D.A.R., G.M.S., A.M.S., B.S.S., S.A.B., F.J.B., and T.E.A. Investigation: S.D., D.L., D.A.R., A.M.S., and T.E.A. Visualization: S.D., D.L., D.A.R., A.M.S., B.S.S., S.A.B., F.J.B., and T.E.A. Funding acquisition: B.S.S., S.A.B., F.J.B., and T.E.A. Project administration: T.E.A. Supervision: B.S.S., F.J.B., and T.E.A. Writing – original draft: S.D. and T.E.A. Writing – review and editing: S.D., D.L., D.A.R., G.M.S., A.M.S., B.S.S., S.A.B., F.J.B., and T.E.A. **Competing interests:** S.D., B.S.S., and T.E.A are inventors on a US patent application (PCT/US2021/037346). All other authors declare that they have no competing interests. **Data and materials availability:** All data are available in the manuscript and the supplementary material; code for the design and generation of print trajectories for the heart valve model is freely accessible at Zenodo (*36*).

SUPPLEMENTARY MATERIALS

science.org/doi/10.1126/science.ade4441
Materials and Methods
Supplementary Text
Figs. S1 to S7
Movies S1 to S3

Submitted 17 August 2022; accepted 17 February 2023
10.1126/science.ade4441

A silicone-based support material eliminates interfacial instabilities in 3D silicone printing

Senthilkumar Duraivel, Dimitri Laurent, Didier A. Rajon, Georg M. Scheutz, Abhishek M. Shetty, Brent S. Sumerlin, Scott A. Banks, Frank J. Bova, and Thomas E. Angelini

Science, **379** (6638), .
DOI: 10.1126/science.ade4441

Overcoming challenges with silicone

Silicone elastomers are used in a wide range of applications because of their resistance to heat, moisture, and chemical agents. However, three-dimensional (3D) printing with silicone is challenging because of the interfacial behavior of the precursors. Duraivel *et al*. present a method to 3D print precise, free-standing, highly detailed objects out of silicone-based materials by using densely packed emulsions surrounded by a silicone oil continuous phase as the support material. This technique allows for precise control over the interfacial tension between the support material and the printing fluid. The authors demonstrated that they could print features as small as four micrometers, as well as mechanically robust, thin-walled, accurate models of human vasculature. —MSL

Science
AAAS

Supplementary Materials for

A silicone-based support material eliminates interfacial instabilities in 3D silicone printing

Senthilkumar Duraivel *et al*.

Corresponding author: Thomas E. Angelini, t.e.angelini@ufl.edu

Science **379**, 1248 (2023)
DOI: 10.1126/science.ade4441

The PDF file includes:

Other Supplementary Material for this manuscript includes the following:

Materials and Methods

Jammed emulsion support material formulation

Inverse emulsions of aqueous droplets in silicone oil were prepared using deionized (DI) water, glycerol (Fisher Scientific), silicone oils (Gelest DMS-T05, 770 g/mol molecular weight; 5 cSt viscosity) and diglycerol surfactant (DOWSIL 5600, cetyl diglyceryl tris(trimethylsiloxy)silylethyl dimethicone). The aqueous droplet phase consists of DI water and glycerol mixed at a 48:52 weight ratio to get a refractive index of 1.397, which is that of the continuous phase. The continuous phase consists of silicone oil mixed with the surfactant; the concentration of the surfactant was fixed at 1% (w/w) relative to the total emulsion weight. Emulsions were formulated by dripping the aqueous phase into the continuous oil phase while homogenizing using an IKA Ultra-Turrax homogenizer; formulations with different volume fractions and homogenization rates were prepared using this protocol. For all the AMULIT printing described in this paper, emulsion formulation with an aqueous phase volume fraction of 0.75 homogenized at 8000 rpm was employed.

Fluorescent PDMS ink synthesis

Reagents and solvents were purchased from commercial sources and used without further purification unless noted otherwise. To formulate a fluorescently labeled PDMS ink for printing, fluorescein (2.00 g, 6.02 mmol), cystamine dihydrochloride (4.07 g, 18.1 mmol), 4-dimethylaminopyridine (DMAP; 0.222 g, 1.81 mmol), and ethylcarbodiimide hydrochloride (EDC·HCl, 3.46 g, 18.1 mmol) were combined in a flame dried round bottom flask under Argon (Ar). At 0 ˚C, dry DMF (30 mL) was added followed by triethylamine (TEA; 5.0 mL, 36 mmol). The reaction was stirred overnight (16 h) and warmed up to room temperature. The reaction mixture was diluted with methanol (MeOH; 15 mL) and DI water (15 mL) and the pH was adjusted to 7 with aqueous HCl (1 M). Dithiothreitol (5.0 g, 32 mmol) was added under Ar and the reaction was stirred overnight (12 h). Upon acidification with aqueous HCl (1 M) to a pH of 3, the product precipitated from the reaction mixture. After centrifugation and drying in vacuo, Fluo-SH was obtained as a red solid (0.82 g; 2.0 mmol; 33% yield) and used without further purification.

Vinyl-terminated PDMS (MW = 28,000 g/mol, Gelest Inc., 2.5 g, 0.089 mmol), and 2,2-dimethoxy-2-phenylacetophenone (DMPA, 0.002 mg, 0.009 mmol) were dissolved in THF (15 mL) in a round bottom flask. Fluo-SH (0.28 g, 0.71 mmol) was added in DMF (0.5 mL), and the solution was sparged with Ar for 15 min. Subsequently, the thiol-ene reaction was initiated with UV light. After 4 h stirring in the UV light the reaction was exposed to oxygen and the solution was diluted with methanol, causing a phase separation with PDMS in the bottom layer. The PDMS layer was collected and residual solvent was removed on a rotary evaporator. The crude product was re-dissolved in hexanes (5 mL) and the solution was filtered through a syringe filter (0.45 μm) to remove any precipitates. This cycle of methanol-induced phase separation followed by filtration in hexanes was repeated three times until the methanol supernatant remained clear. The final product Fluo-PDMS was obtained after drying in vacuo overnight.

Preparation of silicone elastomer inks

Brain aneurysm models were printed using a room temperature vulcanizing (RTV) silicone formulation, Gelest ExSil-100, homogenously mixed at a 100:1 base-to-crosslinker ratio at 3500 rpm for 30 s in a FlackTek DAC 150 SpeedMixer. Barium sulfate powder was added to the silicone ink at 1% (w/w) relative to the total formulation weight to facilitate CT imaging. The formulation was then degassed in vacuum for 5 minutes and then loaded into a BD plastic syringe. Heart valve

model structures were printed using a UV-curable silicone formulation, Momentive UV Electro-225, mixed at 50:1 base-to-crosslinker ratio at 3500 rpm for 30 s; low viscosity silicone oil (Gelest DMS-T07; viscosity, 5 cSt) was added at 10% (w/w) relative to the total formulation weight to lower the viscosity of the silicone ink. Degassed ink was then loaded into a Hamilton Gastight syringe and used for printing. Post-printing, the structures were cured under a 320 – 390 nm UV flood lamp (Sunray) at full power (400 W). Dogbone samples for tensile testing were fabricated using the PlastSil-71 silicone formulation prepared at the manufacturer's recommended mixing ratio. A custom-made Peltier-based syringe cooler was used to increase the pot life of the mixed formulation long enough to accommodate the total print time. Linear structures for measuring the feature size and stability were printed using Smooth-On Mold Max 10 RTV silicone formulation; 5 cSt silicone oil was mixed at 10% (w/w) relative to the total formulation weight to lower the viscosity and degassed before printing.

Brain aneurysm and heart valve model design

To create a realistic model of patient neurovasculature, we employ high resolution cerebral angiography fluoroscopic data collected at the time of cerebral angiography, where the neuro-interventionalist selectively injects non-ionic contrast medium into the internal carotid artery. With complete opacification of the ipsilateral anterior cerebral circulation, the Allura Xper FD20 Xray system (Philips Healthcare, Best, Netherlands) takes 122 images over 4.1 seconds during a 3D rotational prop scan over an arc of 240 degrees. The software reconstructs these images into a 3D model that is sent to a separate workstation for review. The 3D scan is segmented and processed to create a vascular wall by pixel dilation of the segmented image. The resulting image is then converted into a 3D aneurysm model and transformed into a series of 3D printing trajectories.

The 3D aneurysm model was printed in a series of trajectories in such a way that each path can be traced in a seamless spiral path. Each individual trajectory was obtained from PrusaSlicer v2.3.3, an open-source software, as a GCode file; the slicer settings were fixed to spiral trajectory with no top and bottom layer, with 0% infill, and with variable layer height between 300 and 400 micrometers. The obtained GCode files are parsed using a custom-written MATLAB script and are converted into trajectory file formats readable by our custom-built 3D printer. The neurovascular structures are printed, cured, then imaged using a TOSHIBA Acquilion ONE CT scanner, set to have a tube voltage of 120 kVp, an exposure time product of 262.5 mAs, a pitch factor of 0.625, and a volume CT dose index (CTDIvol) of 64.6 mGy.

The heart valve model was designed by using a custom MATLAB script using the dimensions of the human aortic heart valve to design different heart valve features in a continuous spiral path (Fig. S5). The diameter of sinus wall was chosen to be 25 mm, the leaf height was chosen to be 12 mm and the total valve height was chosen to be 25 mm. Cylindrical extensions with a diameter of 12 mm and a height of 3 mm were added to the top and bottom of the model to allow the cured structure to be clamped to fluid tubing during performance testing. The curved root and sinus walls of the valve were programmed as a segment of a sine function, seamlessly joined to the helical cylindrical paths of the tubing attachments. The valve leaflets were designed using helical paths that lay on the intersection of triangular shapes with the valve wall. Following the leaflet trajectory from bottom to top, the apex of each triangular layer lays on a segment of a sine function that begins at the wall and approaches the center of the valve. These path trajectories were generated in the format readable by our custom-built printer.

Summary of silicone inks and corresponding tests.

To highlight the versatility of the AMULIT printing approach, we use six different PDMS ink formulations across nine different tests of printing performance. In the comparisons between aqueous and AMULIT support materials, we use Gelest vinyl-terminated PDMS (DMS-V31), functionalized with fluorescein in our labs. The brain aneurysm model is made from Gelest ExSil-100 (RTV). Momentive UV Electro225 (UV) is used to create the heart valve model and for surface roughness measurements. PlastSil-71 (RTV) is used in tensile tests and fatigue tests. Feature diameter measurements (single time-point and time-course) are performed using Smooth-On Mold Max 10 (RTV). Interfacial tension measurements are performed using Gelest phenyl-PDMS (PMM-5021).

Embedded 3D printing procedure

All the AMULIT printing technique was performed with a custom-made 3D printer made by using a linear stage as a syringe pump (Physik Instrumente) mounted to three linear translations stages (Newport). We fabricated printing needles by pulling glass microcapillaries (1 mm outer diameter) using a pipette puller (David Kopf Instruments). The pulled capillaries were secured to Luer-lock hubs. Additionally, metal needles between 23G and 34G were used. These needles were Luer-locked to the printing syringes, loaded with the silicone ink, and mounted to the syringe pump. Custom-written MATLAB scripts and functions were used to produce precise trajectory paths for the syringe pump and the translation stages, which traces the needle tip along the designed 3D structure within containers containing the AMULIT support material.

Rheological protocols

All rheology characterization of the emulsions were performed using an Anton Paar MCR 702 rheometer, employing a roughened 25 mm parallel plate measurement geometry. Complex moduli were measured in the linear viscoelastic range by performing oscillatory frequency sweeps from 10 Hz to 10^{-3} Hz at a strain amplitude of 1%. The yield stresses of the packed emulsions were determined by measuring the shear stress during unidirectional shear rate sweeps, spanning shear rates from 10^{-2} to 100 s^{-1}. All samples were pre-sheared at 50 s^{-1} for 60 seconds and then allowed to relax for 120 seconds before the rheology measurements.

Imaging methods

Timelapse photographs of the printing process and the photographs of the silicone structures were taken using a Nikon D3100 camera under white LED light illumination with a multi-colored LED light foreground illumination. Micrographs and Z-stack images of the printed features were taken using a Nikon Eclipse Ti-E microscope with a C2 confocal scanning system. Brightfield images of single features were collected using an inverted Nikon Eclipse Ti-E microscope.

Feature diameter measurements

The printed lines are imaged using brightfield microscopy, focusing on the mid-plane of printed features. The images are processed in MATLAB to remove background noise and to invert the intensity distributions. The processed intensity maps are then averaged along the long axis of printed features to create single intensity profiles, as shown in figure 3A. Each intensity profile is fit with a Gaussian function, given by $I(R) = I_0 e^{-(R-\mu)^2/(2\sigma^2)}$, where μ is the peak location and σ controls the width of the function (Fig. 3A). We estimate the feature diameter from the best fit value of σ, given by $d = 4\sigma$.

Tensile and fatigue test methods

Dogbone shaped specimens are printed using a print-nozzle translation speed of v = 2 mm/s and a material deposition rate of Q = 700 μL/hr, corresponding to a feature diameter of 350 μm. All tensile tests were performed using the Instron 5943. The test samples were designed and tested in accordance with the ASTM D412-C specifications and the extension rate for all samples was fixed to 500 mm/min. The stress and strain for the tested samples were calculated from the force and displacement values recorded by the instrument, using the cross-sectional area and the length of the sample in the central region of the dogbone. Plots of stress versus strain on a log-log scale revealed that the linear regime extended up to 20% strain. We fit a line with no offsets to this region of the stress-strain curve to determine the tensile elastic modulus.

Fatigue test specimens were fabricated using the same printing parameters as those used to fabricate tensile specimens (350 μm feature diameter). Fatigue test specimens were fabricated in the shape of rectangular strips with dimensions of 50 mm length, 4.5 mm width, and 2.25 mm thickness. The samples were fatigued in a custom-made reciprocating instrument. The samples strained by ±10% relative to their unstrained state at 2 Hz for 10^5 cycles. During the positive half of each strain cycle, the samples were stretched; during the negative half of each cycle, the samples buckled under the compressive load, bending the specimens. The fatigued samples were then subjected to unidirectional tensile stress as described previously and analyzed with the same fitting procedure. Quantitative comparisons were made to un-fatigued samples (Fig. S7A).

Surface roughness analysis

Sections of the heart valve model were cut from the fully 3D printed models and suspended approximately 170 μm above the microscope cover slip. Rhodamine solutions was wicked between the heart valve section and the cover slip. This procedure oriented the heart valve sections perpendicular to the optical axis of the confocal microscope. Intensity profile along the optical axis is analyzed at each X-Y location in the 3D Z-stack to determine a 2D map of surface locations. Each 2D map spans regions approximately 1 mm across (Fig. 4D,E). We quantify surface roughness by computing the root-mean-square (RMS) distance between each measured surface location and the mean surface location. This quantity is determined from three different regions across the heart valve surface and averaged.

Supplementary Text

Control and characterization of emulsion droplet size

At a single volume fraction, ϕ, the droplet radius, a, is expected to influence jammed emulsion rheology. Thus, to understand the rheological properties and related printing performance of AMULIT support materials, it is critical to measure the statistics of emulsion droplet radius. To measure the sizes of emulsion droplets, we mix the aqueous phase with rhodamine 6G at 10 μM concentration to make emulsions with a fluorescent droplet phase under conditions that will produce candidate AMULIT support materials. These materials are then dispersed and diluted for single-droplet size measurements. Stable emulsions made at different volume fractions, homogenization rates, and continuous phase viscosities are diluted in 1:10 silicone oil containing 1% (w/w) surfactant and imaged with fluorescence microscopy (Fig. S1A). The images are processed using custom written programs in MATLAB. To remove random background noise, we first apply a Gaussian filter with a width of 1 pixel size to the images. The

droplets are then identified by segmenting the smoothed images using Otsu's method. The binary image is then further processed to remove the partial droplet images from the image boundaries, and then eroded and dilated to remove artifacts from remaining noise. We then label the individual non-clustered droplets in the image by only measuring the cross-sectional areas of identified regions having an eccentricity less than 0.6. We then compute effective droplet radius from droplet cross-sectional area, assuming circular droplet geometry. Droplet radii are logarithmically binned and we construct a normalized probability distribution (PDF) of droplet radius (Fig. S1B).

We find that the droplet size distribution is dependent on the homogenization rate, ω, emulsion volume fraction, ϕ, and continuous phase viscosity, η; a higher value of ω, ϕ, or η shifts the distribution toward lower droplet sizes (Fig. S1B). Plots of droplet size distribution resemble the log-normal lineshape. Thus, we fit log-normal functions to the droplet size distributions to determine the median droplet size at each combination of ϕ, ω and η. For example, in the case of an emulsion formulated at ϕ = 0.75, ω = 3000 rpm and η = 5 cSt, we find the median droplet diameter to be 5.38 μm. In the case of an emulsion formulated at ϕ = 0.75, ω = 7000 rpm and η = 5 cSt, we find the median droplet diameter to be 2.75 μm. The measured droplet diameters, 2*a*, for emulsions prepared at different ω collapse to a single curve that weakly decreases with increasing ϕ when the viscous shear stress during homogenization is accounted for (Fig. S1C).

Rheology of Jammed Inverse Emulsions

To formulate a variety of inverse emulsions suitable for AMULIT printing and to identify the best performing support material, we prepare emulsions at different homogenization rates, ω, viscosities, η, and volume fractions, ϕ. We expect to be able to tune the rheological properties by controlling droplet size, *a*, which is controlled by all these variables during the homogenization process. Likewise, we expect ϕ to control the rheological properties independently. To determine the linear shear moduli, *G*' and *G*", of each emulsion formulation, we perform oscillatory frequency sweeps spanning frequencies of 0.001 Hz to 10 Hz, at low strain amplitudes of 1%. To determine the yield stress of each emulsion formulation, we measure the shear stress while performing unidirectional shear rate sweeps, covering shear rates between 100 s^{-1} and 0.001 s^{-1}. We compute the value of the yield stress by fitting the data with the Herschel-Bulkley model, $\sigma = \sigma_y(1 + (\dot{\varepsilon}/\dot{\varepsilon}_c)^p)$, where σ is the measured shear stress, $\dot{\varepsilon}$ is the shear rate, σ_y is the yield stress, $\dot{\varepsilon}_c$ is the shear rate at which the viscous stress equals the yield stress, and *p* is a dimensionless number.

For samples prepared at a single homogenization rate, ω = 8000 rpm, in a continuous phase of silicone oil having a viscosity, η = 5 cSt, we find that the yield stress and the elastic modulus of the emulsion can be tuned by controlling the volume fraction, ϕ (Fig. S2A and S2B). To investigate the dependence of elastic modulus on emulsion volume fraction, ϕ, above a minimal packing fraction, ϕ_0, we determine the value of *G*' at f = 0.1 Hz for emulsions made at a ω = 8000 rpm and different values of ϕ. We find a quadratic increase in storage modulus with increasing with ϕ above ϕ_0 = 0.649 (Fig. S2C). To determine whether this this scaling relationship holds for samples made using the same continuous phase but prepared at different homogenization rates, ω, we re-scaled *G*' from samples homogenized at ω = 4000 rpm and ω = 8000 rpm, multiplying *G*' by the corresponding mean droplet radius, *a*, and plotting them against the adjusted volume fraction, given by $\phi - \phi_0$. We find the two datasets collapse onto the same curve following a quadratic scaling approximately like $(\phi - \phi_0)^2$ (Fig. S2D). The same scaling strategy does not work when comparing emulsions prepared with continuous phases having different viscosities. We

hypothesize this result arises from the interfacial tension varying across samples having different continuous phases. We therefore performed tests at constant ϕ and ω, while varying η. The resulting plots of re-scaled modulus, $G'a$, versus η exhibit an inverse relationship between the two (Fig. S2E). Since G' is a measure of energy storage and not dissipation, and we have accounted for a and ϕ, we believe this result indicates the inverse relationship arises from different interfacial tensions exhibited by the different silicone oils with the aqueous droplets. Finally, we find a universal scaling law between the yield stress, σ_y and elastic modulus G', given by $\sigma_y = 0.005(G')^{1.36}$ for all emulsion samples made with varying volume fractions, homogenization rates, and continuous phase viscosities, showing good predictability of the macroscopic yielding behavior of these packed emulsions (Fig. S2F).

Estimation of Reynolds number during printing

To predict whether irregular flow patterns occur near the printing nozzle within the support material during AMULIT printing, we estimate the Reynold's number, given by $R_e = \rho v d_n / \eta$, where ρ and η are the density and the apparent viscosity of the AMULIT support medium, v is the nozzle translation speed and d_n is the nozzle diameter of the printing needle. For the range of d_n between 0.16 mm and 1 mm, and a range of v between 0.1 mm/s to 20 mm/s, used in this work, we find the span of possible shear rates, approximated as $\dot{\varepsilon} = v / d_n$, to be between 0.1 to 100 s^{-1}. The corresponding apparent viscosity for the support material is determined from the unidirectional shear rate sweep measurements (Fig. S2B) from the relationship $\eta = \sigma / \dot{\varepsilon}$, where σ is the shear stress at the corresponding shear rate. We find the rage of viscosities to be between 0.8 and 150 Pa s. Combining these parameters, we find the range of R_e to be between 10^{-6} and 10^{-2}, which is several orders of magnitude below the threshold value that results in irregular flows near the translating needle.

Refractive Index Matching

To effectively fabricate silicone structures and visualize the printing process using the AMULIT technique, optically clear emulsions are needed. The refractive index (RI) mismatch between water (1.333) and silicone oil (1.399), results in extremely cloudy emulsions (Fig. S3). We mix glycerol to the aqueous phase at a final aqueous phase weight ratio of 48:52 of water and glycerol to match the RI between the two phases, resulting in optically clear emulsions.

Interfacial tension measurements

To determine the interfacial tension between PDMS ink and the AMULIT support medium, and to benchmark the AMULIT technique against other current embedded printing methods, we identify the minimum stable feature diameter, d_{min}, at a given support material yield stress, σ_y. At the threshold of stability, where disruptive interfacial forces balance the stabilizing yield stress of the AMULIT support medium, the feature diameter is given by $d_{min} \approx 2\ \gamma / \sigma_y$, where γ is the interfacial tension. We print features using phenymethylsiloxane-dimethylsiloxane silicone oil (Gelest PMM-5021) as our ink, as it is chemically similar to the PDMS oil used in formulating the support medium while facilitating brightfield imaging of the features due its higher refractive index (Fig. S4A). We print features of different diameters, d, into AMULIT support media having different σ_y, between 0.5 Pa and 5 Pa. We observe the feature stability over 2 hours using brightfield imaging. Creating a map of stable and unstable features in d-σ_y space, we identify a linear boundary having a slope equal to γ (Fig. S4B). We find $\gamma \approx 80$ μN/m which is nearly three orders of magnitude smaller than the previously reported hydrocarbon oil-based support medium.

Modeling Heart Valves

To 3D print a silicone heart valve representative of the human aortic heart valve, we model the print trajectory using custom written MATLAB program. We use the native aortic valve geometric dimensions available from the literature to model the print trajectory. We model the trajectory in such a way that the aorta wall and the valve leaflets can be traced in a seamless spline path (Fig. S5), enabling us to fabricate a uniform-walled structure. We add structural extensions on the top and the bottom of the model, to allow the cured structure to be clamped to fluid tubing during performance testing. The layer height of the model was set at 100 microns and the leaflets were spaced at 1 mm apart from each other; we find these values offer good layer-to-layer adhesion and provide a constant wall thickness throughout the structure. We render the designed print trajectory into a 3D model by converting the cloud points to a mesh using, MeshLab v2020.12, an open-source software. We use this model to evaluate and compare the print trajectory and the print structure with the native aortic heart valve structure.

Stability of 3D printed features over time

To measure the effect of ultra-low interfacial tension leveraged during the AMULIT printing technique on the time-evolution of apparently stable printed features, we print linear features of Smooth-On Mold Max 10 PDMS formulation without any curing agent and analyze the feature width over a period of 2 hours using timelapse imaging obtained through brightfield microscopy. The feature images are processed using the same protocol described in Fig. 3 and the measured feature diameter at the time of printing and two hours post-printing are compared (Fig. S6). The printed features are observed to be stable over time without interfacial instability-related breakups. The negligible decrease in the width of the printed feature is associated to the diffusion of low-viscous formulation components into the support medium; we predict this will be negated during fabrication process as the formulation will be allowed to cure.

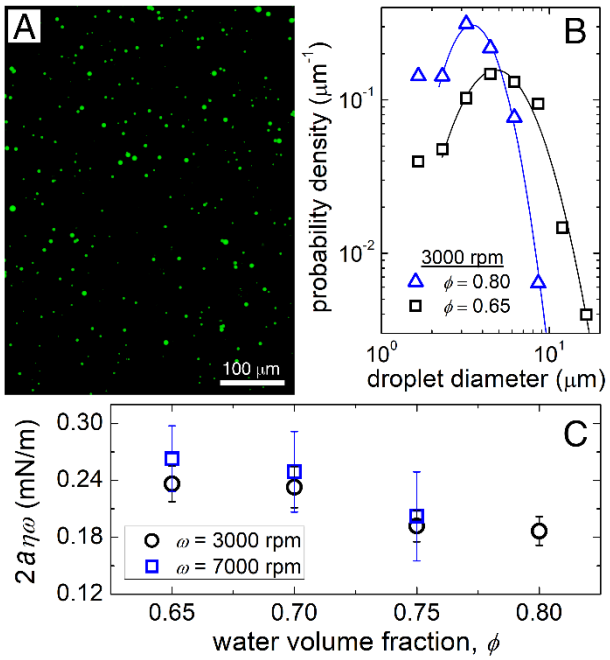

Fig. S1. Measurement of emulsion droplet sizes. (A) Fluorescence microscopic imaging of the emulsion droplets are collected to measure the statistical distribution of droplet sizes. (B) Droplet size distributions follow log-normal statistics with smaller average droplet sizes arising at higher volume fractions, ϕ. (C) Measurements of the characteristic droplet radii, a, prepared at different homogenization rates, ω, collapse when the viscous shear-stress during homogenization is taken into account (η is the silicone oil viscosity).

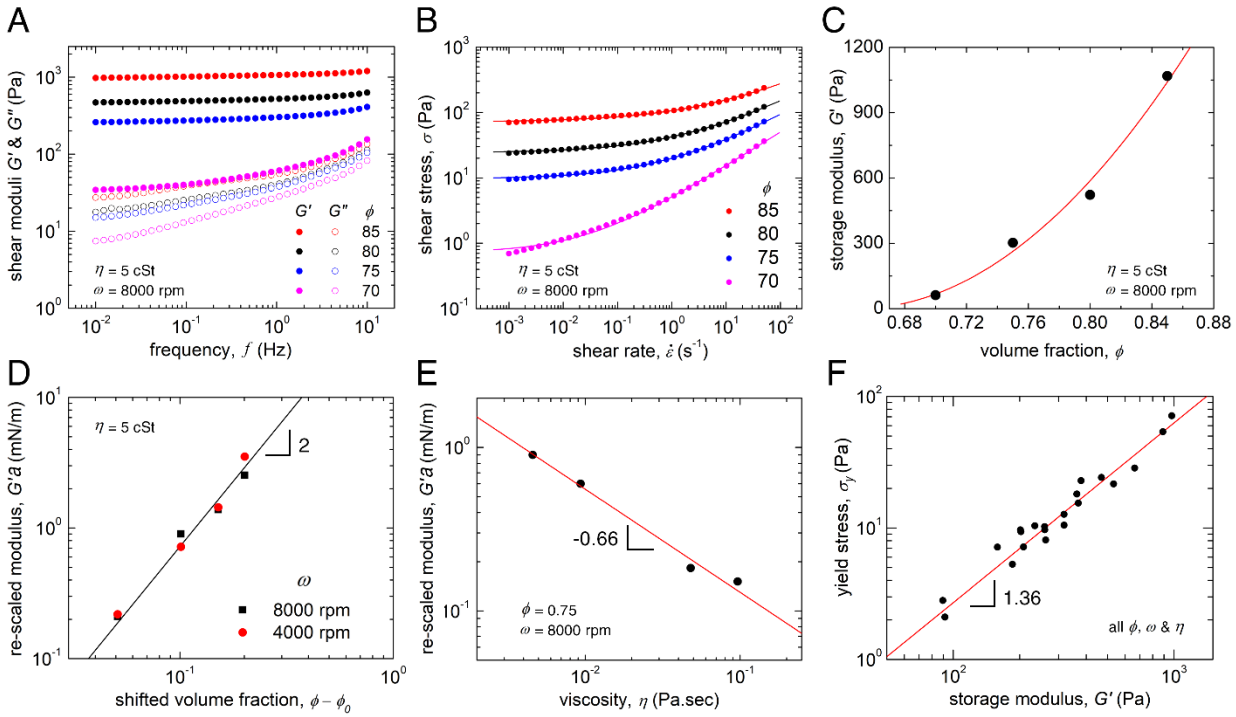

Fig. S2. Rheological characterization of jammed emulsions. (A) Small amplitude oscillatory frequency sweeps are used to determine the shear elastic moduli, G', and viscous moduli, G'', with increasing volume fraction, ϕ, for samples prepared at a single homogenization rate, ω, in a continuous phase of silicone oil having a viscosity, η. (B) To determine the yield stress of these samples, unidirectional shear rate sweeps are performed; lines passing through data-points are fits of the Herschel-Bulkley model. (C) The storage modulus at a frequency of $f = 0.1$ Hz scales approximately quadratically above a minimally-packed volume fraction of $\phi_0 = 0.649$. (D) G' from samples prepared using the same continuous phase but with different homogenization rates collapse onto the same curve when re-scaled by the mean droplet radius, a, and plotted versus the volume fraction above close-packing, $\phi - \phi_0$, scaling approximately like $(\phi - \phi_0)^2$. (E) For a given volume fraction and homogenization rate, the rescaled modulus decreases with increasing viscosity of the silicone oil continuous phase, which likely arises from the different oils exhibiting different levels of interfacial tension against the aqueous phase. (F) A plot of the yield stress versus G' for emulsions prepared at different volume fractions, homogenization rates, and continuous phase viscosities reveals that samples of all combinations lay close to a universal scaling curve given by $\sigma_y = 0.005(G')^{1.36}$.

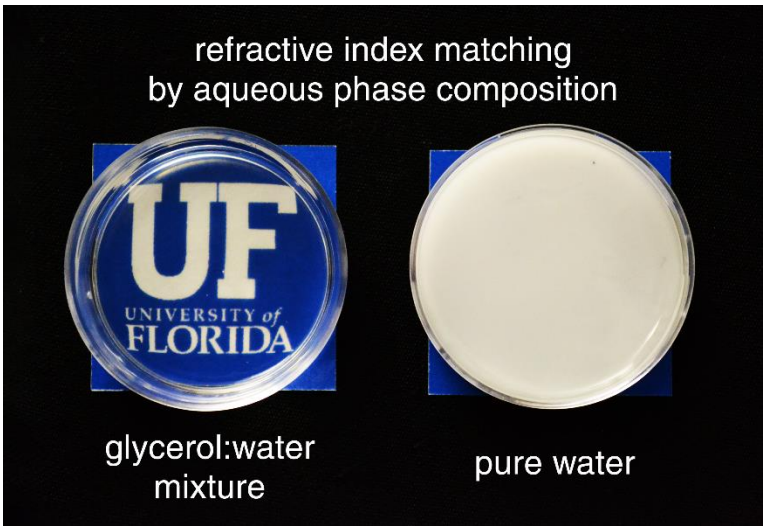

Fig. S3. Optically clear emulsion formulations. To eliminate cloudiness that arises from the refractive index mismatch between the aqueous droplets and the silicone oil continuous phase (right panel), we formulate the droplets from a mixture of water and glycerol at a composition that matches the refractive index of the silicone oil continuous phase; this formulation results in optically clear emulsions (left panel).

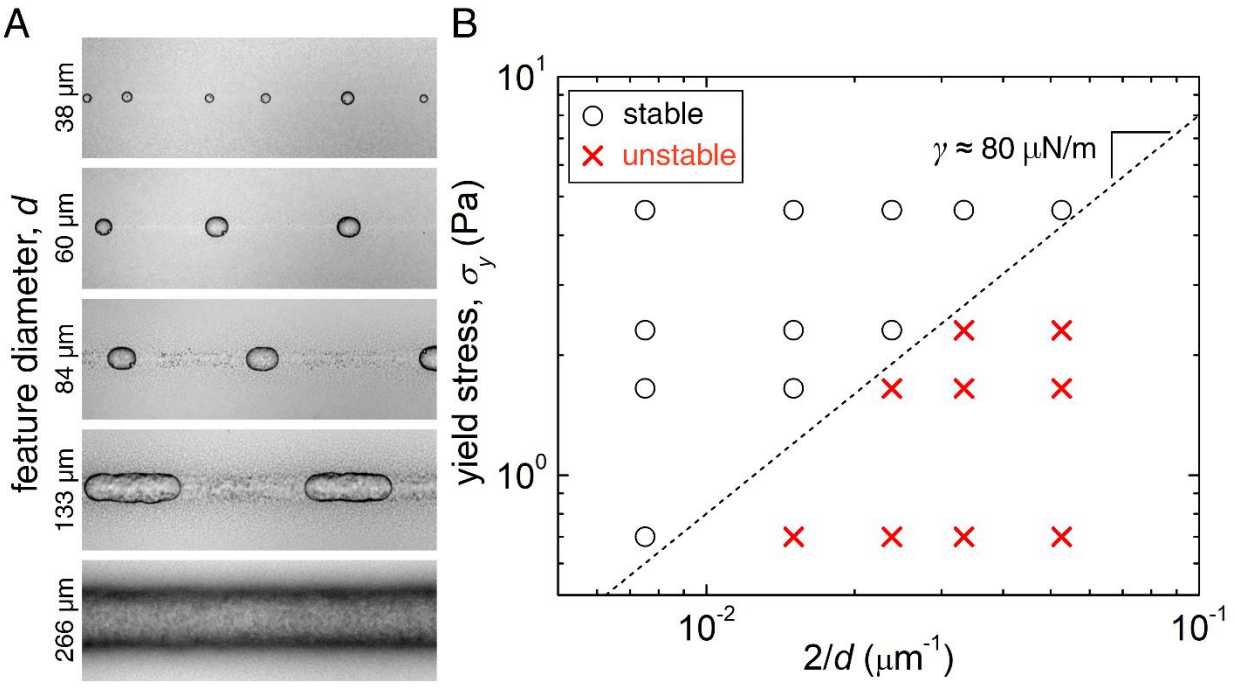

Fig. S4. Effective interfacial tension measurements. To determine the interfacial tension between silicone ink and the AMULT support medium, we print features having different diameters, d, into support media having different yield stresses, σ_y. For each value of yield stress, a different minimum stable feature size, d_{min}, is expected, given by $d_{min} \approx 2\,\gamma / \sigma_y$, where γ is the interfacial tension. (A) For packed emulsions having $\sigma_y = 0.7$ Pa, the printed features having a diameter of 133 µm break-up into smaller droplets as the surface stresses created by the ink-support material interface are higher enough to yield the support material. (B) A stability state diagram of features having different diameters printed into AMULIT support media having different yield stresses shows the transition from stable features (black circles) into unstable droplets (red crosses). From the linear boundary between these two regimes, we estimate the interfacial tension to be approximately 80 µN/m.

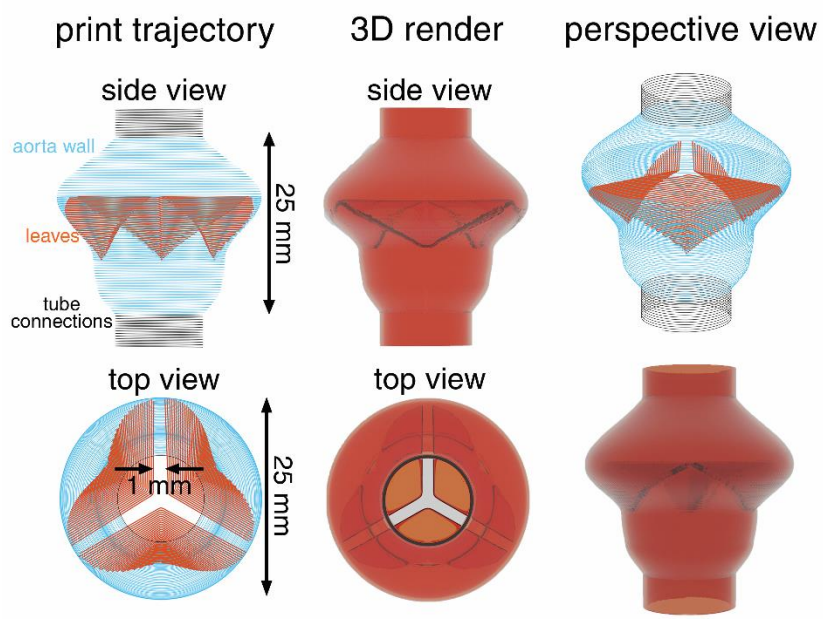

Fig. S5. Modeling the aortic heart valve. Print trajectory of the model heart valve was designed by using typical geometric dimensions of the human aortic heart valve available in the literature. The print trajectory is a single-trace spline path which enables a seamless and efficient printing of the sinus wall and valve leaflets with uniform wall thickness. Cylindrical extensions are modeled at the top and bottom of the heart valve to enable connections to tubes for structure-performance testing of the cured structure. 3D render of the print trajectory as a solid mesh compares well with the native aortic heart valve.

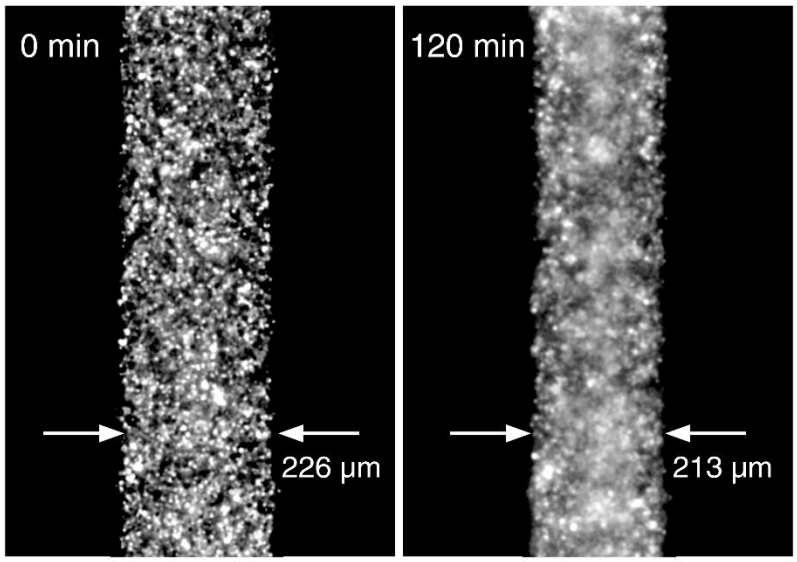

Fig. S6. Feature stability measurements. To test the effect of ultra-low interfacial tension on the printed feature stability, we print linear PDMS features without curing agents and analyze their stability with timelapse imaging. We image the feature using brightfield microscopy, process the image to remove background noise, and invert the intensity distribution. The feature width is estimated by using the same approach used in Fig. 2A. We observe the printed feature to be stable over a period of two hours, without any interfacial instability related breaks and with a negligible change in width due to the diffusion.

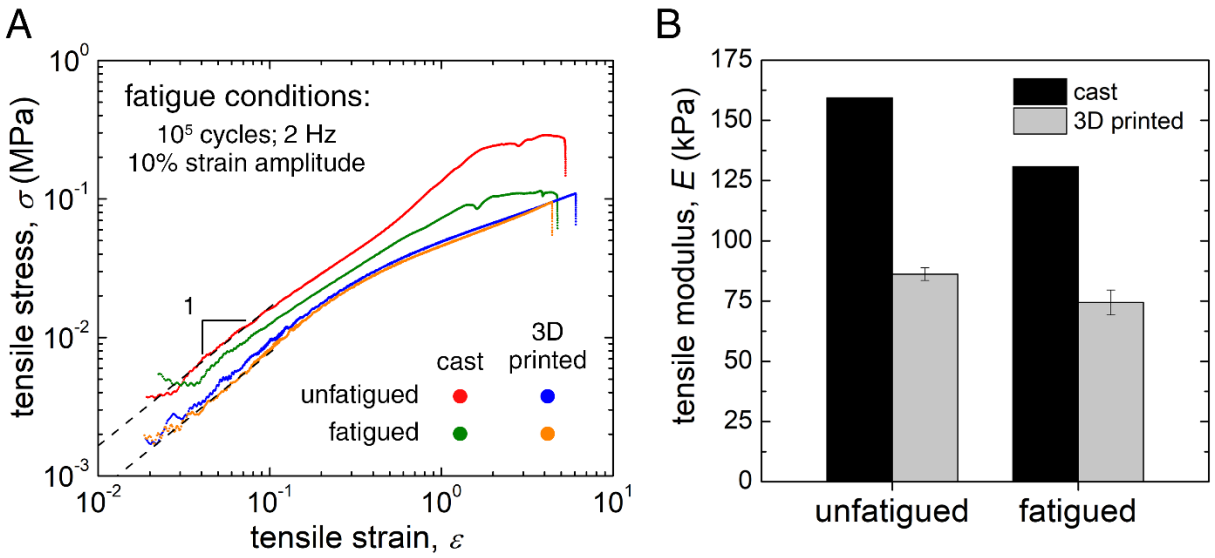

Fig. S7. Fatigue tests of silicone structures. Silicone tensile specimens are subject to cyclic strains of ±10% amplitude at a frequency of 2 Hz for 10^5 cycles, then subject to unidirectional tensile stress until failure. (A) Tensile stress-strain curves of fatigued and unfatigued samples that are 3D printed are compared with their molded counterparts; the samples show linear stress-strain relationships at low strains (B) Fatigued samples exhibit an elastic modulus slightly lower than unfatigued samples. The cast samples exhibit an 18% reduction in modulus and the 3D printed samples exhibit a 14% reduction (error bars correspond to the standard deviation across three replicas).

Movie S1. 3D printing a brain aneurysm model. Time-lapse photography of a neurovascular model being 3D printed with Smooth-On silicone formulation. The optically clear emulsion allows for easy observation of the printing process and the rheology of the AMULIT support medium enables the translating needle to seamlessly move while trapping the silicone ink in the deposited trajectory. Duration: 6.5 hours.

Movie S2. 3D scan and 2D slices of the brain aneurysm model. Graphic render of the printed neurovascular model obtained through CT imaging shows the complexity of the branched structure. The progression of slices through XZ and XY planes of the CT scan shows the hollow structure and the thin walls obtained when employing AMULIT printing.

Movie S3. Fluid pumped through a 3D printed silicone heart valve. Real time time-lapse video shows transvalvular flow during the cardiac cycle simulated by coupling the silicone heart valve to a fluid pump, where the thin leaflets of the valve can be seen opening and closing in response to systolic and diastolic flows.

References and Notes

1. C. R. Kensil, U. Patel, M. Lennick, D. Marciani, Separation and characterization of saponins with adjuvant activity from *Quillaja saponaria* Molina cortex. *J. Immunol.* **146**, 431–437 (1991). doi:10.4049/jimmunol.146.2.431 Medline

2. A. King, "Soapbark reaches out to fill essential role in some vaccine recipes" (Chemistry World, 2022); https://www.chemistryworld.com/news/soapbark-branches-out-to-fill-essential-role-in-vaccine-recipes/4015836.article.

3. G. C. Kite, M. J. Howes, M. S. Simmonds, Metabolomic analysis of saponins in crude extracts of *Quillaja saponaria* by liquid chromatography/mass spectrometry for product authentication. *Rapid Commun. Mass Spectrom.* **18**, 2859–2870 (2004). doi:10.1002/rcm.1698 Medline

4. A. S. Grandón, B. M. Espinosa, D. L. Ríos, O. M. Sánchez, C. K. Sáez, S. V. Hernández, A. J. Becerra, Variation of saponin contents and physiological status in *Quillaja saponaria* under different environmental conditions. *Nat. Prod. Commun.* **8**, 1697–1700 (2013). Medline

5. L. P. Iglesias, J. G. Castro, V. A. Artze-Vargas, R. O. Peredo, Production of biomass in ultra high density plantations, U.S. Patent No. 11,254,699 (2022).

6. S. Copaja, C. Blackburn, R. Carmona, Variation of saponin contents in *Quillaja saponica* Molina. *Wood Sci. Technol.* **37**, 103–108 (2003). doi:10.1007/s00226-002-0150-8

7. K. Miettinen, S. Iñigo, L. Kreft, J. Pollier, C. De Bo, A. Botzki, F. Coppens, S. Bak, A. Goossens, The TriForC database: A comprehensive up-to-date resource of plant triterpene biosynthesis. *Nucleic Acids Res.* **46**, D586–D594 (2018). doi:10.1093/nar/gkx925 Medline

8. K. Malhotra, J. Franke, Cytochrome P450 monooxygenase-mediated tailoring of triterpenoids and steroids in plants. *Beilstein J. Org. Chem.* **18**, 1289–1310 (2022). doi:10.3762/bjoc.18.135 Medline

9. A. Jozwiak, P. D. Sonawane, S. Panda, C. Garagounis, K. K. Papadopoulou, B. Abebie, H. Massalha, E. Almekias-Siegl, T. Scherf, A. Aharoni, Plant terpenoid metabolism co-opts a component of the cell wall biosynthesis machinery. *Nat. Chem. Biol.* **16**, 740–748 (2020). doi:10.1038/s41589-020-0541-x Medline

10. Y. Li, A. Leveau, Q. Zhao, Q. Feng, H. Lu, J. Miao, Z. Xue, A. C. Martin, E. Wegel, J. Wang, A. Orme, M. D. Rey, M. Karafiátová, J. Vrána, B. Steuernagel, R. Joynson, C. Owen, J. Reed, T. Louveau, M. J. Stephenson, L. Zhang, X. Huang, T. Huang, D. Fan, C. Zhou, Q. Tian, W. Li, Y. Lu, J. Chen, Y. Zhao, Y. Lu, C. Zhu, Z. Liu, G. Polturak, R. Casson, L. Hill, G. Moore, R. Melton, N. Hall, B. B. H. Wulff, J. Doležel, T. Langdon, B. Han, A. Osbourn, Subtelomeric assembly of a multi-gene pathway for antimicrobial defense compounds in cereals. *Nat. Commun.* **12**, 2563 (2021). doi:10.1038/s41467-021-22920-8 Medline

11. R. Xu, G. C. Fazio, S. P. Matsuda, On the origins of triterpenoid skeletal diversity. *Phytochemistry* **65**, 261–291 (2004). doi:10.1016/j.phytochem.2003.11.014 Medline

12. One Thousand Plant Transcriptomes Initiative, One thousand plant transcriptomes and the phylogenomics of green plants. *Nature* **574**, 679–685 (2019). doi:10.1038/s41586-019-1693-2 Medline

13. T. Schlotterbeck, M. Castillo–Ruiz, H. Cañon–Jones, R. S. Martín, The use of leaves from young trees of *Quillaja saponaria* (Molina) plantations as a new source of saponins. *Econ. Bot.* **69**, 262–272 (2015). doi:10.1007/s12231-015-9320-0

14. H. Hayashi, P. Huang, A. Kirakosyan, K. Inoue, N. Hiraoka, Y. Ikeshiro, T. Kushiro, M. Shibuya, Y. Ebizuka, Cloning and characterization of a cDNA encoding β-amyrin synthase involved in glycyrrhizin and soyasaponin biosyntheses in licorice. *Biol. Pharm. Bull.* **24**, 912–916 (2001). doi:10.1248/bpb.24.912 Medline

15. K. Miettinen, J. Pollier, D. Buyst, P. Arendt, R. Csuk, S. Sommerwerk, T. Moses, J. Mertens, P. D. Sonawane, L. Pauwels, A. Aharoni, J. Martins, D. R. Nelson, A. Goossens, The ancient CYP716 family is a major contributor to the diversification of eudicot triterpenoid biosynthesis. *Nat. Commun.* **8**, 14153 (2017). doi:10.1038/ncomms14153 Medline

16. M. Carelli, E. Biazzi, F. Panara, A. Tava, L. Scaramelli, A. Porceddu, N. Graham, M. Odoardi, E. Piano, S. Arcioni, S. May, C. Scotti, O. Calderini, *Medicago truncatula* CYP716A12 is a multifunctional oxidase involved in the biosynthesis of hemolytic saponins. *Plant Cell* **23**, 3070–3081 (2011). doi:10.1105/tpc.111.087312 Medline

17. G. Polturak, Z. Liu, A. Osbourn, New and emerging concepts in the evolution and function of plant biosynthetic gene clusters. *Curr. Opin. Green Sustain. Chem.* **33**, 100568 (2022). doi:10.1016/j.cogsc.2021.100568

18. S. Garcia, T. Garnatje, O. Hidalgo, G. Mas de Xaxars, J. Pellicer, I. Sánchez-Jiménez, D. Vitales, J. Vallès, First genome size estimations for some eudicot families and genera. *Collect. Bot.* **29**, 7–16 (2010). doi:10.3989/collectbot.2010.v29.001

19. S. B. Cannon, M. R. McKain, A. Harkess, M. N. Nelson, S. Dash, M. K. Deyholos, Y. Peng, B. Joyce, C. N. Stewart Jr., M. Rolf, T. Kutchan, X. Tan, C. Chen, Y. Zhang, E. Carpenter, G. K.-S. Wong, J. J. Doyle, J. Leebens-Mack, Multiple polyploidy events in the early radiation of nodulating and nonnodulating legumes. *Mol. Biol. Evol.* **32**, 193–210 (2015). doi:10.1093/molbev/msu296 Medline

20. S. A. Kautsar, H. G. Suarez Duran, K. Blin, A. Osbourn, M. H. Medema, plantiSMASH: Automated identification, annotation and expression analysis of plant biosynthetic gene clusters. *Nucleic Acids Res.* **45**, W55–W63 (2017). doi:10.1093/nar/gkx305 Medline

21. T. Louveau, A. Osbourn, The sweet side of plant-specialized metabolism. *Cold Spring Harb. Perspect. Biol.* **11**, a034744 (2019). doi:10.1101/cshperspect.a034744 Medline

22. S. Rahimi, J. Kim, I. Mijakovic, K. H. Jung, G. Choi, S.-C. Kim, Y.-J. Kim, Triterpenoid-biosynthetic UDP-glycosyltransferases from plants. *Biotechnol. Adv.* **37**, 107394 (2019). doi:10.1016/j.biotechadv.2019.04.016 Medline

23. S. Y. Chung, H. Seki, Y. Fujisawa, Y. Shimoda, S. Hiraga, Y. Nomura, K. Saito, M. Ishimoto, T. Muranaka, A cellulose synthase-derived enzyme catalyses 3-*O*-glucuronosylation in saponin biosynthesis. *Nat. Commun.* **11**, 5664 (2020). doi:10.1038/s41467-020-19399-0 Medline

24. J. D. Fleck, A. H. Betti, F. P. da Silva, E. A. Troian, C. Olivaro, F. Ferreira, S. G. Verza, Saponins from *Quillaja saponaria* and *Quillaja brasiliensis*: Particular chemical characteristics and biological activities. *Molecules* **24**, 171 (2019). doi:10.3390/molecules24010171 Medline

25. Y. Yin, J. Huang, X. Gu, M. Bar-Peled, Y. Xu, Evolution of plant nucleotide-sugar interconversion enzymes. *PLOS ONE* **6**, e27995 (2011). doi:10.1371/journal.pone.0027995 Medline

26. Y. Kallberg, U. Oppermann, B. Persson, Classification of the short-chain dehydrogenase/reductase superfamily using hidden Markov models. *FEBS J.* **277**, 2375–2386 (2010). doi:10.1111/j.1742-4658.2010.07656.x Medline

27. Y. Yoshida, Y. Nakano, T. Nezu, Y. Yamashita, T. Koga, A novel NDP-6-deoxyhexosyl-4-ulose reductase in the pathway for the synthesis of thymidine diphosphate-D-fucose. *J. Biol. Chem.* **274**, 16933–16939 (1999). doi:10.1074/jbc.274.24.16933 Medline

28. T. Oka, T. Nemoto, Y. Jigami, Functional analysis of *Arabidopsis thaliana* RHM2/MUM4, a multidomain protein involved in UDP-D-glucose to UDP-L-rhamnose conversion. *J. Biol. Chem.* **282**, 5389–5403 (2007). doi:10.1074/jbc.M610196200 Medline

29. H. Moummou, Y. Kallberg, L. B. Tonfack, B. Persson, B. van der Rest, The plant short-chain dehydrogenase (SDR) superfamily: Genome-wide inventory and diversification patterns. *BMC Plant Biol.* **12**, 219 (2012). doi:10.1186/1471-2229-12-219 Medline

30. H. W. Choi, B.-G. Lee, N. H. Kim, Y. Park, C. W. Lim, H. K. Song, B. K. Hwang, A role for a menthone reductase in resistance against microbial pathogens in plants. *Plant Physiol.* **148**, 383–401 (2008). doi:10.1104/pp.108.119461 Medline

31. T. Czechowski, E. Forestier, S. H. Swamidatta, A. D. Gilday, A. Cording, T. R. Larson, D. Harvey, Y. Li, Z. He, A. J. King, G. D. Brown, I. A. Graham, Gene discovery and virus-induced gene silencing reveal branched pathways to major classes of bioactive diterpenoids in *Euphorbia peplus*. *Proc. Natl. Acad. Sci. U.S.A.* **119**, e2203890119 (2022). doi:10.1073/pnas.2203890119 Medline

32. J. Ziegler, S. Voigtländer, J. Schmidt, R. Kramell, O. Miersch, C. Ammer, A. Gesell, T. M. Kutchan, Comparative transcript and alkaloid profiling in *Papaver* species identifies a short chain dehydrogenase/reductase involved in morphine biosynthesis. *Plant J.* **48**, 177–192 (2006). doi:10.1111/j.1365-313X.2006.02860.x Medline

33. M. Parakkottil Chothi, G. A. Duncan, A. Armirotti, C. Abergel, J. R. Gurnon, J. L. Van Etten, C. Bernardi, G. Damonte, M. Tonetti, Identification of an L-rhamnose synthetic pathway in two nucleocytoplasmic large DNA viruses. *J. Virol.* **84**, 8829–8838 (2010). doi:10.1128/JVI.00770-10 Medline

34. S. Guo, L. Kenne, Characterization of some *O*-acetylated saponins from *Quillaja saponaria* Molina. *Phytochemistry* **54**, 615–623 (2000). doi:10.1016/S0031-9422(00)00161-8 Medline

35. S. Guo, L. Kenne, Structural studies of triterpenoid saponins with new acyl components from *Quillaja saponaria* Molina. *Phytochemistry* **55**, 419–428 (2000). doi:10.1016/S0031-9422(00)00340-X Medline

36. M. Pabst, J. Grass, R. Fischl, R. Léonard, C. Jin, G. Hinterkörner, N. Borth, F. Altmann, Nucleotide and nucleotide sugar analysis by liquid chromatography-electrospray ionization-mass spectrometry on surface-conditioned porous graphitic carbon. *Anal. Chem.* **82**, 9782–9788 (2010). doi:10.1021/ac101975k Medline

37. W. Kreis, A. Hensel, U. Stuhlemmer, Cardenolide biosynthesis in foxglove 1. *Planta Med.* **64**, 491–499 (1998). doi:10.1055/s-2006-957500

38. M. Manni, M. R. Berkeley, M. Seppey, F. A. Simão, E. M. Zdobnov, BUSCO Update: Novel and streamlined workflows along with broader and deeper phylogenetic coverage for scoring of eukaryotic, prokaryotic, and viral genomes. *Mol. Biol. Evol.* **38**, 4647–4654 (2021). doi:10.1093/molbev/msab199 Medline

39. D. J. MacKenzie, M. A. McLean, S. Mukerji, M. Green, Improved RNA extraction from woody plants for the detection of viral pathogens by reverse transcription-polymerase chain reaction. *Plant Dis.* **81**, 222–226 (1997). doi:10.1094/PDIS.1997.81.2.222 Medline

40. F. Sainsbury, E. C. Thuenemann, G. P. Lomonossoff, pEAQ: Versatile expression vectors for easy and quick transient expression of heterologous proteins in plants. *Plant Biotechnol. J.* **7**, 682–693 (2009). doi:10.1111/j.1467-7652.2009.00434.x Medline

41. C. Engler, R. Kandzia, S. Marillonnet, A one pot, one step, precision cloning method with high throughput capability. *PLOS ONE* **3**, e3647 (2008). doi:10.1371/journal.pone.0003647 Medline

42. E. Weber, C. Engler, R. Gruetzner, S. Werner, S. Marillonnet, A modular cloning system for standardized assembly of multigene constructs. *PLOS ONE* **6**, e16765 (2011). doi:10.1371/journal.pone.0016765 Medline

43. F. Sainsbury, P. Saxena, K. Geisler, A. Osbourn, G. P. Lomonossoff, Using a virus-derived system to manipulate plant natural product biosynthetic pathways. *Methods Enzymol.* **517**, 185–202 (2012). doi:10.1016/B978-0-12-404634-4.00009-7 Medline

44. J. Reed, M. J. Stephenson, K. Miettinen, B. Brouwer, A. Leveau, P. Brett, R. J. M. Goss, A. Goossens, M. A. O'Connell, A. Osbourn, A translational synthetic biology platform for rapid access to gram-scale quantities of novel drug-like molecules. *Metab. Eng.* **42**, 185–193 (2017). doi:10.1016/j.ymben.2017.06.012 Medline

45. M. G. Grabherr, B. J. Haas, M. Yassour, J. Z. Levin, D. A. Thompson, I. Amit, X. Adiconis, L. Fan, R. Raychowdhury, Q. Zeng, Z. Chen, E. Mauceli, N. Hacohen, A. Gnirke, N. Rhind, F. di Palma, B. W. Birren, C. Nusbaum, K. Lindblad-Toh, N. Friedman, A. Regev, Full-length transcriptome assembly from RNA-Seq data without a reference genome. *Nat. Biotechnol.* **29**, 644–652 (2011). doi:10.1038/nbt.1883 Medline

46. B. J. Haas, A. Papanicolaou, M. Yassour, M. Grabherr, P. D. Blood, J. Bowden, M. B. Couger, D. Eccles, B. Li, M. Lieber, M. D. MacManes, M. Ott, J. Orvis, N. Pochet, F. Strozzi, N. Weeks, R. Westerman, T. William, C. N. Dewey, R. Henschel, R. D. LeDuc, N. Friedman, A. Regev, *De novo* transcript sequence reconstruction from RNA-seq using the Trinity platform for reference generation and analysis. *Nat. Protoc.* **8**, 1494–1512 (2013). doi:10.1038/nprot.2013.084 Medline

47. A. M. Bolger, M. Lohse, B. Usadel, Trimmomatic: A flexible trimmer for Illumina sequence data. *Bioinformatics* **30**, 2114–2120 (2014). doi:10.1093/bioinformatics/btu170 Medline

48. D. Mapleson, L. Venturini, G. Kaithakottil, D. Swarbreck, Efficient and accurate detection of splice junctions from RNA-seq with Portcullis. *Gigascience* **7**, ••• (2018). doi:10.1093/gigascience/giy131 Medline

49. L. Venturini, S. Caim, G. G. Kaithakottil, D. L. Mapleson, D. Swarbreck, Leveraging multiple transcriptome assembly methods for improved gene structure annotation. *Gigascience* **7**, giy093 (2018). doi:10.1093/gigascience/giy093 Medline

50. M. Stanke, B. Morgenstern, AUGUSTUS: A web server for gene prediction in eukaryotes that allows user-defined constraints. *Nucleic Acids Res.* **33**, W465–W467 (2005). doi:10.1093/nar/gki458 Medline

51. R. Patro, G. Duggal, M. I. Love, R. A. Irizarry, C. Kingsford, Salmon provides fast and bias-aware quantification of transcript expression. *Nat. Methods* **14**, 417–419 (2017). doi:10.1038/nmeth.4197 Medline

52. A. Hallab, "Protein function prediction using phylogenomics, domain architecture analysis, data integration, and lexical scoring," dissertation, Rheinische Friedrich-Wilhelms-Universität Bonn (2015).

53. S. Ou, W. Su, Y. Liao, K. Chougule, J. R. A. Agda, A. J. Hellinga, C. S. B. Lugo, T. A. Elliott, D. Ware, T. Peterson, N. Jiang, C. N. Hirsch, M. B. Hufford, Benchmarking transposable element annotation methods for creation of a streamlined, comprehensive pipeline. *Genome Biol.* **20**, 275 (2019). doi:10.1186/s13059-019-1905-y Medline

54. M.-D. Rey, G. Moore, A. C. Martín, Identification and comparison of individual chromosomes of three accessions of *Hordeum chilense*, *Hordeum vulgare*, and *Triticum aestivum* by FISH. *Genome* **61**, 387–396 (2018). doi:10.1139/gen-2018-0016 Medline

55. R. C. Edgar, MUSCLE: Multiple sequence alignment with high accuracy and high throughput. *Nucleic Acids Res.* **32**, 1792–1797 (2004). doi:10.1093/nar/gkh340 Medline

56. A. Stamatakis, RAxML version 8: A tool for phylogenetic analysis and post-analysis of large phylogenies. *Bioinformatics* **30**, 1312–1313 (2014). doi:10.1093/bioinformatics/btu033 Medline

57. M. I. Love, W. Huber, S. Anders, Moderated estimation of fold change and dispersion for RNA-seq data with DESeq2. *Genome Biol.* **15**, 550 (2014). doi:10.1186/s13059-014-0550-8 Medline

58. R Core Team, "R: A language and environment for statistical computing" (R Foundation for Statistical Computing, 2021); www.R-project.org/.

59. D. Hoffmeister, J. Yang, L. Liu, J. S. Thorson, Creation of the first anomeric D/L-sugar kinase by means of directed evolution. *Proc. Natl. Acad. Sci. U.S.A.* **100**, 13184–13189 (2003). doi:10.1073/pnas.100.23.13184 Medline

60. J. C. Errey, B. Mukhopadhyay, K. P. R. Kartha, R. A. Field, Flexible enzymatic and chemo-enzymatic approaches to a broad range of uridine-diphospho-sugars. *Chem. Commun.* **23**, 2706–2707 (2004). doi:10.1039/b410184g Medline

61. V. Martinez, M. Ingwers, J. Smith, J. Glushka, T. Yang, M. Bar-Peled, Biosynthesis of UDP-4-keto-6-deoxyglucose and UDP-rhamnose in pathogenic fungi *Magnaporthe grisea* and *Botryotinia fuckeliana*. *J. Biol. Chem.* **287**, 879–892 (2012). doi:10.1074/jbc.M111.287367 Medline

62. M. Rejzek, B. Mukhopadhyay, C. Q. Wenzel, J. S. Lam, R. A. Field, Direct oxidation of sugar nucleotides to the corresponding uronic acids: TEMPO and platinum-based procedures. *Carbohydr. Res.* **342**, 460–466 (2007). doi:10.1016/j.carres.2006.10.016 Medline

63. B. A. Wagstaff, M. Rejzek, S. Kuhaudomlarp, L. Hill, I. Mascia, S. A. Nepogodiev, H. C. Dorfmueller, R. A. Field, Discovery of an RmlC/D fusion protein in the microalga *Prymnesium parvum* and its implications for NDP-β-l-rhamnose biosynthesis in microalgae. *J. Biol. Chem.* **294**, 9172–9185 (2019). doi:10.1074/jbc.RA118.006440 Medline

64. R. Behmüller, I. C. Forstenlehner, R. Tenhaken, C. G. Huber, Quantitative HPLC-MS analysis of nucleotide sugars in plant cells following off-line SPE sample preparation. *Anal. Bioanal. Chem.* **406**, 3229–3237 (2014). doi:10.1007/s00216-014-7746-3 Medline

65. J. E. Lunn, R. Feil, J. H. Hendriks, Y. Gibon, R. Morcuende, D. Osuna, W.-R. Scheible, P. Carillo, M.-R. Hajirezaei, M. Stitt, Sugar-induced increases in trehalose 6-phosphate are correlated with redox activation of ADPglucose pyrophosphorylase and higher rates of starch synthesis in *Arabidopsis thaliana*. *Biochem. J.* **397**, 139–148 (2006). doi:10.1042/BJ20060083 Medline

66. M. Rejzek, L. Hill, E. S. Hems, S. Kuhaudomlarp, B. A. Wagstaff, R. A. Field, Profiling of sugar nucleotides. *Methods Enzymol.* **597**, 209–238 (2017). doi:10.1016/bs.mie.2017.06.005 Medline

67. A. E. Wilson, L. Tian, Phylogenomic analysis of UDP-dependent glycosyltransferases provides insights into the evolutionary landscape of glycosylation in plant metabolism. *Plant J.* **100**, 1273–1288 (2019). doi:10.1111/tpj.14514 Medline

68. S. Guo, L. Kenne, L. N. Lundgren, B. Rönnberg, B. G. Sundquist, Triterpenoid saponins from *Quillaja saponaria*. *Phytochemistry* **48**, 175–180 (1998). doi:10.1016/S0031-9422(97)00716-4 Medline

69. H. Tang, J. E. Bowers, X. Wang, R. Ming, M. Alam, A. H. Paterson, Synteny and collinearity in plant genomes. *Science* **320**, 486–488 (2008). doi:10.1126/science.1153917 Medline